Effects of radius ratio on annular centrifugal Rayleigh-Bénard convection

Dongpu Wang,[1] Hechuan Jiang,[1,*] Shuang Liu,[1] Xiaojue Zhu,[2] and Chao Sun[1,3]

[1] *Center for Combustion Energy, Key Laboratory for Thermal Science and Power Engineering of MoE, and Department of Energy and Power Engineering, Tsinghua University, 100084 Beijing, China.*

[2] *Max Planck Institute for Solar System Research, Justus-von-Liebig-Weg 3, 37077 Göttingen, Germany*

[3] *Department of Engineering Mechanics, School of Aerospace Engineering, Tsinghua University, 100084 Beijing, China*

(Dated: January 6, 2022)

We report on a three-dimensional direct numerical simulation study of flow structure and heat transport in the annular centrifugal Rayleigh-Bénard convection (ACRBC) system, with cold inner and hot outer cylinders corotating axially, for the Rayleigh number range Ra $\in [10^6, 10^8]$ and radius ratio range $\eta = R_i/R_o \in [0.3, 0.9]$. This study focuses on the dependence of flow properties on the radius ratio η. The temperature and velocity fields reveal that different curvatures of the inner and outer cylinders of the ACRBC system lead to asymmetric movements of hot and cold plumes under the action of Coriolis force, resulting in the formation of zonal flow. The physical mechanism of zonal flow is verified by the dependence of the drift frequency of the large-scale circulation rolls and the space- and time-averaged azimuthal velocity on η. We find that the larger η is, the weaker the zonal flow becomes. We show that the heat transport efficiency increases with η. It is also found that the bulk temperature deviates from the arithmetic mean temperature and the deviation increases as η decreases. This effect can be explained by a simple model that accounts for the curvature effects and the radially-dependent centrifugal force in ACRBC.

INTRODUCTION

Turbulent convection is ubiquitous in nature and in many industrial processes. Examples include the convective flows in the Earth's mantle [1] and outer core [2], in the atmospheric motion [3, 4], in the ocean [5], and in rotational machines [6]. Many of these convection phenomena occur under rapid rotation of the system [7, 8]. Rayleigh-Bénard convection (RBC), a fluid layer heated from below and cooled from above, is a classical and idealized paradigm for the study of thermally driven turbulent flows [9–15]. The main issues for thermal turbulence studies include the dynamics of turbulent structures and the scaling relation between the heat transport, in the dimensionless form, Nusselt number Nu, and thermally driven force, in the dimensionless form, Rayleigh number Ra. Recently a novel system similar to classical RBC, Annular Centrifugal RBC (ACRBC) system with cold inner and hot outer cylinders corotating axially, has been proposed [16–18]. By exploiting strong centrifugal force through rapid rotation, the intensity of the thermal driving can be significantly enhanced.

In ACRBC, Jiang et al. [17] found that the convective rolls revolve around the rotating center in prograde direction, signifying the emergence of zonal flow, which may be related to the effects of Coriolis force and the different curvatures of the two cylinders. In astrophysical and geophysical studies, by using a rotating cylindrical annulus with conical end surfaces, Busse and his collaborators [19–22] also observed zonal flow phenomenon. According to the topographic-β approximation [23], the strength and direction of the zonal flow in their system depend on the radial gradient of the axial fluid column height. By using a spherical shell model with a radius ratio of 0.9, Heimpel et al. [24] found that zonal flow in the equatorial latitude of Jupiter is prograde with respect to the planet, which is consistent with the actually observed results of Jupiter [25], but the width of equatorial zonal flow does not coincide with the predictions of Rhines scale [26]. The physical mechanism of zonal flow in ACRBC and how it is affected by the curvatures of the two cylinders [17] deserve further study.

In classical turbulent RBC, the effects of aspect ratio Γ on the Nusselt number Nu have been extensively studied

[9, 27–30] and it is found that heat transport efficiency has a great relevance on Γ when it is smaller than 1 [28]. Huang et al. [29, 30] investigated the effects of lateral confinement on heat transport in quasi-2D turbulent RBC and found that narrow lateral width of the convection cell induces the increase of the heat transfer efficiency. In high-Reynolds number Taylor-Couette (TC) turbulence, Grossmann et al. [31] analyzed multiple sets of data from the previous experiments and direct numerical simulations, and found that in the range of radius ratio 0.5-0.909, as the radius ratio increases, the amplitude of TC Nusselt number Nu_ω (the dimensionless angular velocity flux) first increases, and then saturates when the radius ratio is greater than 0.7, indicating that larger radius ratio can achieve higher momentum transport efficiency. Therefore, it is of vital importance to study the effects of geometry on the heat transport efficiency of the ACRBC system, and it can also give insights for the design of rotating machinery [32–34].

We notice that Pitz et al. [35], Kang et al. [16] have studied effects of the radius ratio on the centrifugal buoyancy driven flow, but they mainly focused on the dependence of the critical Rayleigh number $\mathrm{Ra_c}$ and the critical wavenumber ω_c of convection onset through linear stability analysis and numerical simulation. For higher Rayleigh number Ra in the turbulent regime, to the best of our knowledge few attentions have been paid to systematically studying the effects of radius ratio. To fill this gap, we present a systematic investigation of the dynamics of zonal flow and heat transfer properties in the turbulent regime of the ACRBC system with radius ratio from 0.3 to 0.9 by means of high-resolution three-dimensional (3D) direct numerical simulation (DNS). Will the geometric effects in ACRBC be similar to that in RBC or in TC? Answering this question is the major objective in this study.

The remainder of this manuscript is organized as follows. In § 2, we give a brief description of the governing equations and the numerical model. The results are presented and analyzed in § 3, which is divided into three parts, § 3.1 describes the dynamics of zonal flow in ACRBC and explains the physical mechanism of it. In § 3.2, we show the dependence of heat transfer on radius ratio, and discuss the physical reasons. Remarkably asymmetric mean temperature fields are found in ACRBC and predicted by a theoretical model, which are discussed in § 3.3. Finally, we summarize our findings in § 4.

NUMERICAL SETTINGS

Flow setup

We consider a fluid bounded by cold inner and hot outer cylinders, which corotate axially as shown in figure 1. The governing equations are derived from Navier-Stokes equations under the Boussinesq approximation in a rotating reference frame, which are expressed as:

$$\nabla \cdot \mathbf{u} = 0 \ , \tag{1}$$

$$\frac{\partial \theta}{\partial t} + \mathbf{u} \cdot \nabla \theta = \frac{1}{\sqrt{RaPr}} \nabla^2 \theta \ , \tag{2}$$

$$\frac{\partial \mathbf{u}}{\partial t} + \mathbf{u} \cdot \nabla \mathbf{u} = -\nabla p + \mathrm{Ro}^{-1} \hat{\boldsymbol{\omega}} \times \mathbf{u} + \sqrt{\frac{Pr}{Ra}} \nabla^2 \mathbf{u} - \theta \frac{2(1-\eta)}{(1+\eta)} \mathbf{r} \ , \tag{3}$$

where $\widehat{\boldsymbol{\omega}}$ is the unit vector pointing in the direction of the angular velocity, $\boldsymbol{u}$ is the velocity vector normalized by the free-fall velocity $U \equiv \sqrt{\omega^2 \frac{(R_o+R_i)}{2} \alpha \Delta L}$, t is the dimensionless time normalized by L/U, and θ is the temperature normalized by Δ. Here, as defined in figure 1, ω denotes the angular velocity of the system. R_o and R_i are the radius of the outer and inner cylinders, respectively. α,ν,κ are isobaric thermal expansion coefficient, kinematic viscosity and thermal diffusivity of the fluid, respectively. Δ and L are the temperature difference ($\Delta \equiv \theta_{hot} - \theta_{cold}$) and the gap ($L \equiv R_o - R_i$) between the two cylinders. The coordinate system ϕ, z, r refer to the streamwise (azimuthal), spanwise (axial) and wall-normal (radial) directions.

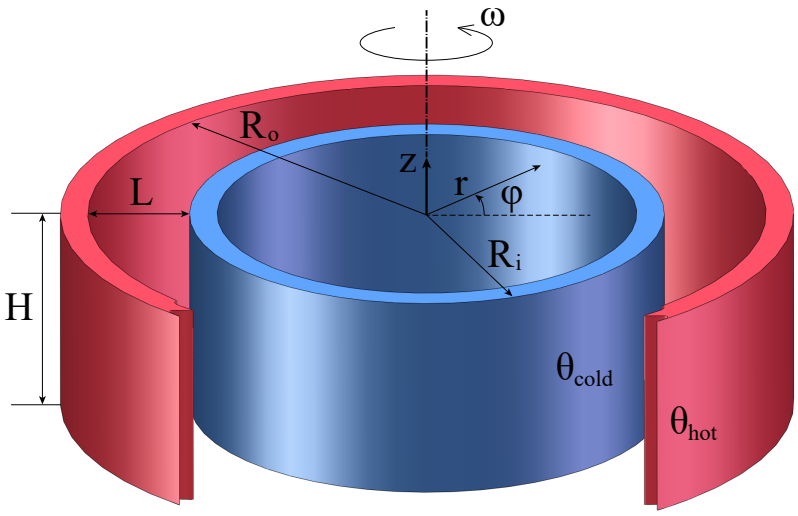

FIG. 1: Schematic diagram of the flow configuration. ω is the angular velocity of the system. All cases in this paper set the angular velocity unit vector $\widehat{\boldsymbol{\omega}} = +1$, that is, the system rotates counterclockwise. R_o, R_i, H and L are the inner radius of the outer cylinder, the outer radius of the inner cylinder, the height of the cylindrical annulus, and the gap width between the two cylinders, respectively. θ_{hot} and θ_{cold} denote the temperature of the outer and inner walls.

The above dimensionless governing equations reveal that ACRBC is mainly controlled by four dimensionless parameters. Similar to classical RBC, Rayleigh number defined as

$$\mathrm{Ra} = \frac{1}{2}\omega^2(R_o + R_i)\alpha\Delta L^3/(\nu\kappa)\ , \tag{4}$$

and Prandtl number $\mathrm{Pr} = \nu/\kappa$ characterize buoyancy-driven strength and physical properties of the convecting fluid. Two additional control parameters are $\mathrm{Ro}^{-1} = \omega L/U$ and $\eta = R_i/R_o$, which measure Coriolis force effects and geometric properties. The key response parameter is the Nusselt number given by

$$\mathrm{Nu} = \frac{J}{J_{con}} = \frac{\langle v_r\theta\rangle_{\phi,z,t} - \kappa\frac{\partial}{\partial r}\langle\theta\rangle_{\phi,z,t}}{\kappa\Delta(r\cdot ln(\eta))^{-1}}\ , \tag{5}$$

where J, J_{con}, v_r and θ denote the total heat flux, the heat flux through pure thermal conduction, the radial velocity and temperature of a certain point, respectively. $\langle ...\rangle_{\phi,z,t}$ denotes taking average over the ϕz-plane and time.

Direct numerical simulations

Numerical simulations are performed using an energy-conserving second-order finite-difference code, which has been described detailedly in literature [17, 36–38]. Thus, here we introduce briefly and just give some main features. Table I documented in appendix lists all the specific simulation parameters. For all cases, no-slip boundary conditions for velocity and constant temperature boundary conditions are adopted at surfaces of inner and outer cylinders. Periodic boundary conditions are imposed on $\boldsymbol{u}$ and θ in the z-direction. The aspect ratio ($\Gamma = H/L$) for most cases is set $\Gamma = 1$, but for high Ra cases (i.e. $\mathrm{Ra} > 10^7$), Γ is reduced to 0.5 even 0.25. Furthermore, for large Ra and $0.6 \le \eta \le 0.9$, the azimuthal domain is reduced from a whole circle ($\phi_0 = 1$) to $\phi_0 = 1/2,\ 1/4,\ 1/8$. The flow domain at least contains a pair of convection rolls to ensure the statistical stability. It is found that such an arrangement will not have considerable impact on Nu and zonal flow.

Adequate resolutions are ensured for all simulations and we have performed a posteriori check of spatial and temporal resolutions to guarantee to resolve all relevant scales. As shown in table I, the ratio of maximum grid spacing Δ_g

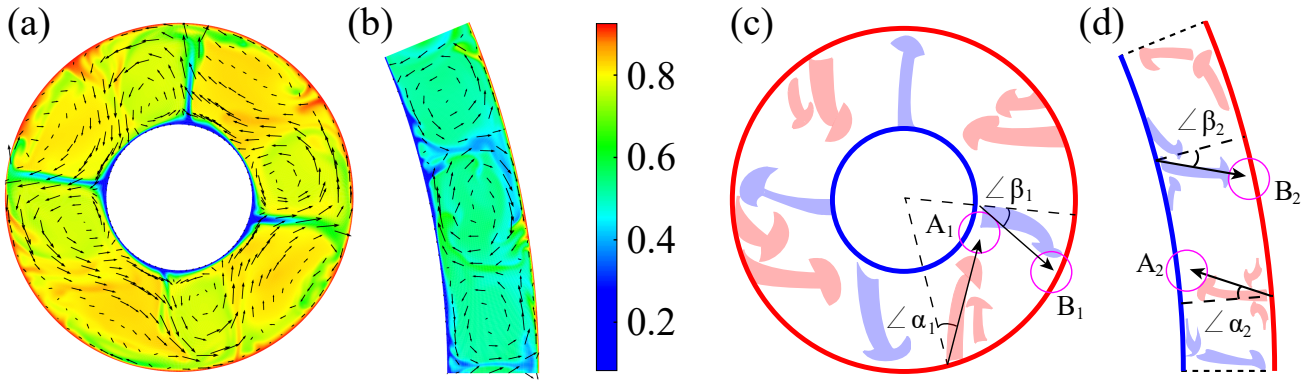

FIG. 2: Typical snapshots of instantaneous temperature fields, superposed by the velocity vectors for $\eta = 0.4$ (a) and $\eta = 0.9$ (b) at $\mathrm{Ra} = 10^7$, $\mathrm{Ro}^{-1} = 1$ and $\mathrm{Pr} = 4.3$. (c,d) Corresponding sketches to (a) and (b), which show the motions of cold (blue) and hot (red) plumes.

in the bulk region to the Kolmogorov scale estimated by the global criterion $\eta_K = \frac{L\mathrm{Pr}^{1/2}}{[\mathrm{Ra}(\mathrm{Nu}-1)]^{1/4}} \cdot [\frac{(1+\eta)\ln(\eta)}{2(\eta-1)}]^{1/4}$ [17] is smaller than 0.7 ($\Delta_g/\eta_K < 0.7$). We have also compared Δ_g with the Batchelor scale $\eta_B = \eta_K \mathrm{Pr}^{-1/2}$ [39] for each case (not shown here) and we have $\Delta_g/\eta_B < 1.4$. Furthermore, the clipped Chebychev-type clustering grids adopted in the radial direction ensure the spatial resolution within BLs. There are at least 8 grid points inside thermal BLs and 10 grid points inside viscous BLs. We use the Courant–Friedrichs–Lewy (CFL) conditions to check temporal resolution [37, 40, 41], i.e. the CFL number is smaller than 0.8 for all simulations to ensure computational stability. τ_{avg} is the averaging time for Nusselt number. For simulation convergence, each case is run for about 100 free-fall time units to discard initial transients, and we obtain the Nu by averaging over an additional $\tau_{avg} \geq 80$ and over the Nusselt numbers $\mathrm{Nu_{in}}$ and $\mathrm{Nu_{out}}$ at the inner and outer walls. One way for statistical convergence is when the difference of Nu between inner and outer walls $\epsilon_{\mathrm{Nu}} = |\mathrm{Nu_{in}} - \mathrm{Nu_{out}}|/\mathrm{Nu}$ is small and acceptable [42, 43]. For most cases, ϵ_{Nu} is less than 1% and the maximum of ϵ_{Nu} is about 1.73%, as shown in table I.

Explored parameter space

In the present study, we aim at studying the geometric effects on ACRBC systematically. The simulations covered a radius ratio η range [0.3, 0.9] and a Ra range [10^6, 10^8]. Pr was fixed at 4.3 corresponding to the working fluids of water at 40°C. Ro^{-1} was fixed at 1, that is because when $\mathrm{Ro}^{-1} \ll 1$, the rotation effect is too weak; while when $\mathrm{Ro}^{-1} \gg 1$, the turbulence is suppressed, and the flow becomes quasi-2D state. In order to study the joint effect of rotation and buoyancy driving, all cases adopt a moderate $\mathrm{Ro}^{-1} = 1$. And besides, all the results in this paper set the angular velocity unit vector $\widehat{\boldsymbol{\omega}} = +1$, that is, the system rotates counterclockwise.

RESULTS AND DISCUSSION

Zonal flow

As mentioned in [17], the convection rolls in ACRBC revolve in prograde direction around the axis with a faster rotation rate than the background rotation of the experimental system, which is the so-called zonal flow. The mechanisms of zonal flow and the responses of the dynamics of zonal flow to η and Ra are discussed in § 3.1.1. Next we present some statistical analyses of zonal flow, i.e. the frequency of the net rotation of the convection rolls and the strength of zonal flow $\langle v_\phi \rangle_{V,t}$ in § 3.1.2, where $\langle ... \rangle_{V,t}$ denotes the average over time and over whole volume.

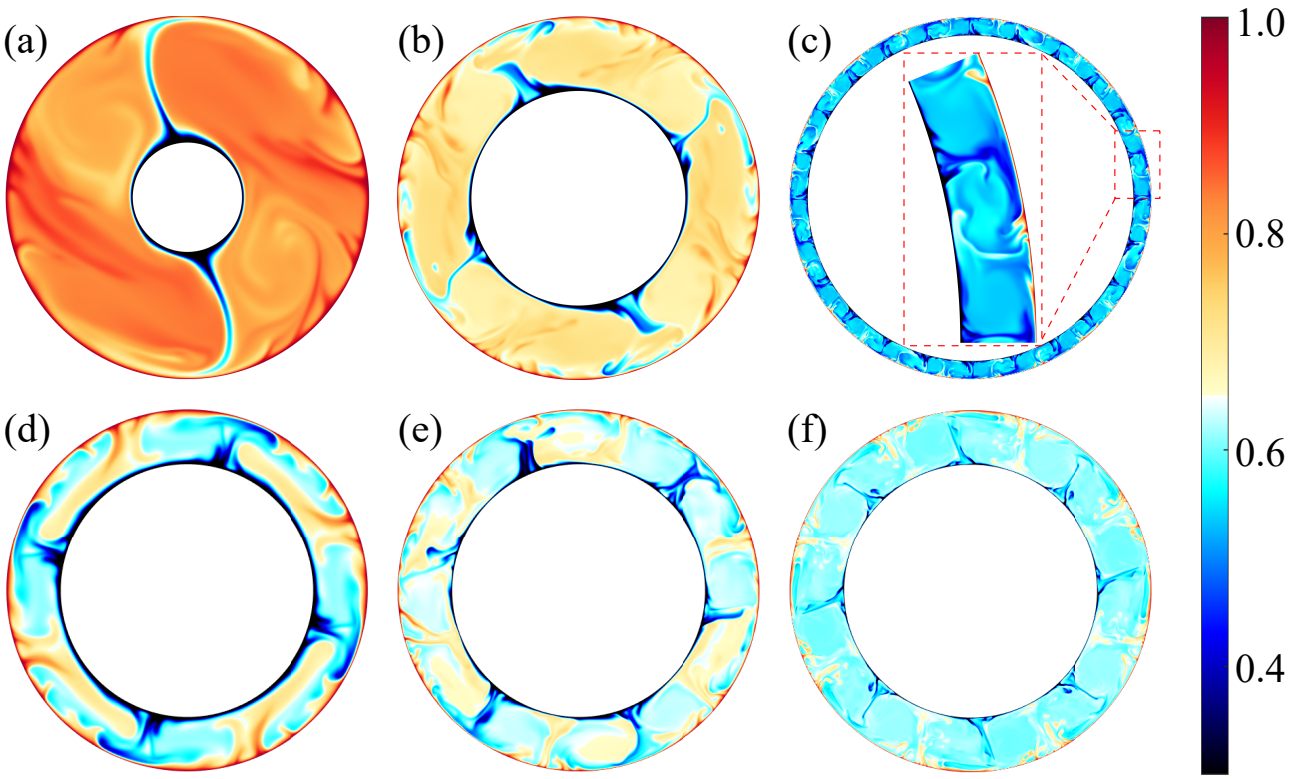

FIG. 3: (a-c) Instantaneous temperature fields on a ϕr-plane for $\eta = 0.3$, 0.6, 0.9 at $\mathrm{Ra} = 10^7$, $\mathrm{Ro}^{-1} = 1$ and $\mathrm{Pr} = 4.3$. (d-f) Instantaneous temperature fields for $\mathrm{Ra} = 10^6$, 10^7, 10^8 at $\eta = 0.7$, $\mathrm{Ro}^{-1} = 1$ and $\mathrm{Pr} = 4.3$. All figures share the same colorbar.

Dynamics of zonal flow

Akin to the classical RBC, the direction of the temperature gradient is parallel to the centrifugal buoyancy in ACRBC. As the temperature difference or the rotation rate increases, the flow will gradually become unstable and convection appears when Ra is higher than critical $\mathrm{Ra_c}$ [35] of convection onset. When $\mathrm{Ra} \gtrsim 10^6$ [16], the flow transitions to be turbulent in the bulk and we will focus on the turbulent convection regime.

In ACRBC, under the rapid rotation of the system, Coriolis force emerges and plays an important role. As shown in figure 2, driven by the Coriolis force, the cold and hot plumes should both have deflected to the right side from the initial direction. The deflected angle of hot plumes ($\angle\alpha$) is roughly equal to the deflected angle of cold plumes ($\angle\beta$). Considering the centrifugal buoyancy is relatively large near the outer cylinder, the deflected angle is slightly large for the hot plumes. However, because of the different curvatures of the inner and outer cylinders (see figure 2(a,c), $\eta = 0.4$), the hot plumes deflect and then impact close to the region $\mathrm{A_1}$ where the cold plumes are ejected, whereas the distance between the impacting region $\mathrm{B_1}$ of the cold plumes and the emitting region of hot plumes is relatively large. Consequently, the hot plumes win and push the overall flow to move counterclockwise. Some cold plumes even deflect to the left side due to the impact of hot plumes. For comparison, the difference between the curvatures of the hot and cold walls is small at $\eta = 0.9$ (see figure 2(b,d)) and both the impacting regions $\mathrm{A_2}$ and $\mathrm{B_2}$ are far away from the ejecting positions of cold and hot plumes, respectively. Thus, zonal flow becomes weaker with η increasing. Figures 3(a-c) show the instantaneous temperature fields for different radius ratios η at $\mathrm{Ra} = 10^7$. When $\eta = 0.3$ (figure 3(a), also see Supplementary Movies 1), the deflected distance of hot plumes are remarkably larger than the cold plumes. When $\eta = 0.6$ (figure 3(b), also see Supplementary Movies 2), the asymmetric movements of cold and hot plumes still could not be ignored. Hot plumes can impact on the root region of the cold plumes, on the contrary the impacting region of cold plumes cannot affect the hot plumes directly. When $\eta = 0.9$ (figure 3(c), also see Supplementary Movies

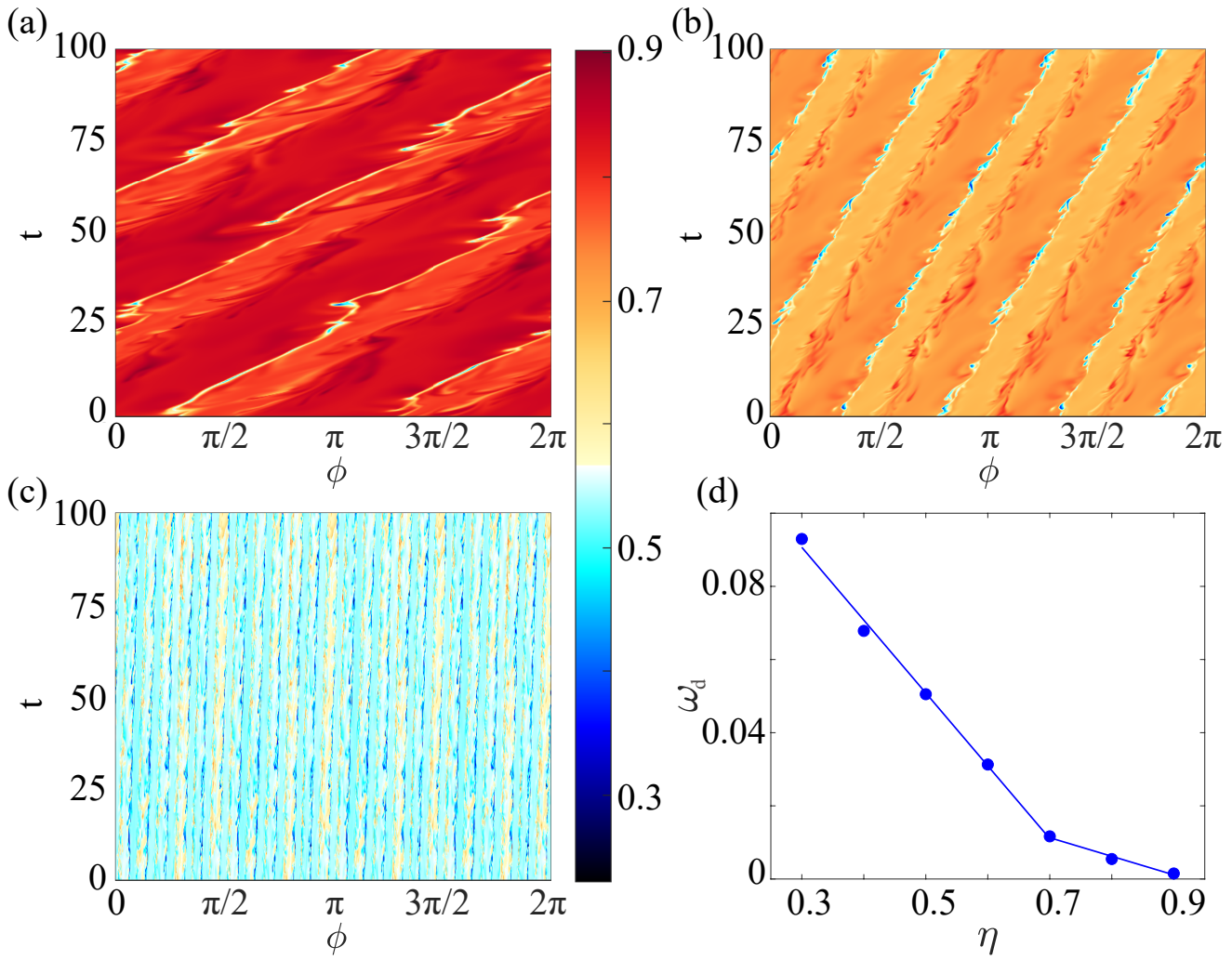

FIG. 4: Azimuth-time temperature contours at the mid-radius and mid-axial position for (a) $\eta = 0.3$, (b) $\eta = 0.6$ and (c) $\eta = 0.9$ at $\mathrm{Ra} = 10^7$. All temperature fields share the same colorbar. (d) Drift frequency ω_d of the convection rolls versus η at $\mathrm{Ra} = 10^7$, where ω_d is the drift angle (radian) per dimensionless time t. The solid lines are the best linear fits of $\omega_d(\eta)$ for $0.3 \leq \eta \leq 0.7$ and $0.7 \leq \eta \leq 0.9$, respectively.

3), the movements of cold and hot plumes are almost symmetric, and there are several pairs of large scale circulation (LSC) rolls without distinct azimuthal movement, which is similar to the classical RBC.

Figures 3(d-f) demonstrate the influences of Ra on flow structures for $\eta = 0.7$. As we know, for classical RBC the aspect ratio of convection rolls approximately equals to one without the confinement effects of sidewalls, which is almost consistent with the case of $\mathrm{Ra} = 10^8$ in ACRBC (see figure 3(f)). However, we find that the wavenumber decreases with the decrease of Ra. This is because for small Ra case, the centrifugal force is relatively small and the flow is under the control of Coriolis force. Hence, the thermal boundary layers (BLs) develop along the wall and are hard to detach to form a convection roll. On the contrary, the strong centrifugal buoyancy in high Ra case will prompt the detachment of thermal plumes from boundary layers to form more convection rolls. And for the same reason, the deflection of the plume in figure 3(f) is significantly weaker compared to figure 3(d).

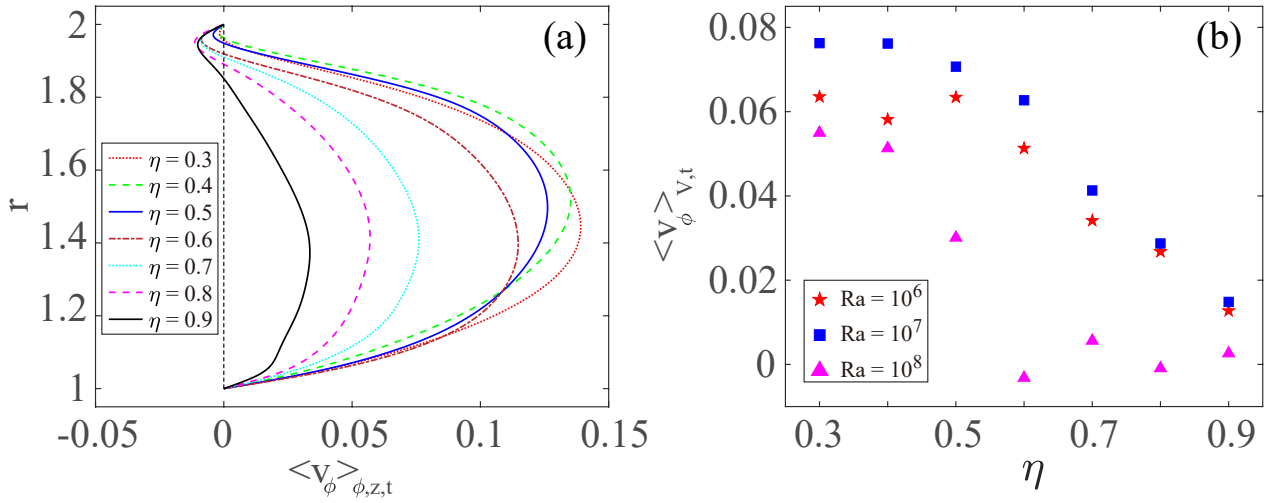

FIG. 5: (a) Azimuthal velocity profiles averaged azimuthally, axially and by time along the radial direction for different η at $\mathrm{Ra} = 10^7$. (b) Mean azimuthal velocity $\langle v_\phi \rangle_{V,t}$ as a function of η for different Ra.

Quantitative analysis of zonal flow

Figures 4(a-c) are the azimuth-time temperature contours at the mid-radius and mid-height position for $\eta = 0.3$, 0.6 and 0.9, respectively, which show that the convection rolls revolve in prograde direction. And besides, the convection rolls drift at a nearly constant rate with high frequency oscillations. Similar effects have also been reported in [35]. Figure 4(d) suggests that the drift frequency ω_d decreases with η increasing (averaged over 100 free-fall time units), where ω_d is defined as the azimuthal movement (radian) of convection rolls per free-fall time unit in the rotating frame. It is found that $\omega_d = -0.05\eta + 0.05$ for $0.7 \leq \eta \leq 0.9$, while it gives a notably steeper slope with $\omega_d = -0.2\eta + 0.15$ for $0.3 \leq \eta \leq 0.7$. This change of the slope of ω_d versus η indicates the influence of curvature effects on the drift frequency of convection rolls is more significant at small η.

Since when there is no systematic deflections of plumes, one would expect that $\langle v_\phi \rangle_{\phi,z,t}$ vanishes. $\langle v_\phi \rangle_{\phi,z,t}$ can reflect the asymmetric extent of the motion of cold and hot plumes. As shown in figure 5(a), with the decrease of η, the positive $\langle v_\phi \rangle_{\phi,z,t}$ (reflects the deflection of hot plumes) is larger and the negative part (reflects the deflection of cold plumes) is smaller in absolute values. Figure 5(b) shows that for each fixed Ra, space- and time-averaged azimuthal velocity all decrease as η increases basically. Thus, the drift of LSC rolls is directly linked to the asymmetric motion of cold and hot plumes. In addition, we find that at moderate Ra ($\mathrm{Ra} = 10^7$), zonal flow is the strongest. When $\mathrm{Ra} = 10^6$, the velocity of plumes is slow due to the weak buoyancy; while when $\mathrm{Ra} = 10^8$, the deflection of plumes is weak as a consequence of strong buoyancy. So the zonal flow driven by the plumes for both cases is relatively weak. We also note that when $\eta \lesssim 0.5$ for $\mathrm{Ra} = 10^6$ and 10^7 or $\eta \lesssim 0.4$ for $\mathrm{Ra} = 10^8$ (figure 5(b)), $\langle v_\phi \rangle_{V,t}$ no longer increases remarkably as η decreases, which is probably a consequence of the increase of the gap width of the convection cell. Long distance to reach the opposite surfaces results in the reduction of the strength of plumes and $\langle v_\phi \rangle_{V,t}$ reaches saturation.

Heat transport

Figure 6(a) shows Nu as a function of Ra for $0.3 \leq \eta \leq 0.9$. When $\eta = 0.3$ or 0.4, Nu(Ra) can be described with a power law $\mathrm{Nu} \sim \mathrm{Ra}^\gamma$ with a scaling exponent γ of 0.28 ± 0.01 (see figure 6(b)). Whereas for $\eta \gtrsim 0.5$, it is found that γ increases significantly, and then gradually becomes saturated to 0.32 ± 0.02. Inset of figure 6(a) shows

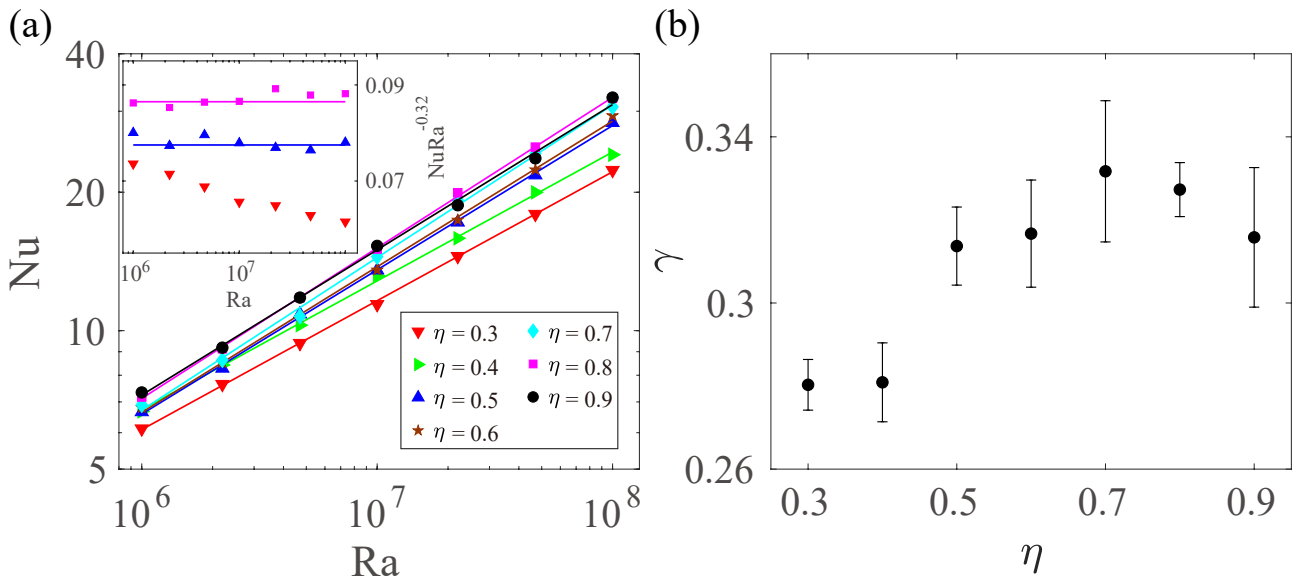

FIG. 6: (a) Nusselt number Nu as a function of Rayleigh number Ra for different η. The inset shows $\mathrm{NuRa}^{-0.32} \sim \mathrm{Ra}$ for $\eta = 0.3, 0.5, 0.8$. (b) Scaling exponents γ obtained by fitting $\mathrm{Nu} \sim \mathrm{Ra}^{\gamma}$ as a function of η. Errorbar is the range of fitting exponent within 95% confidence interval.

$\mathrm{NuRa}^{-0.32}$ as a function of Ra, also suggesting that when $\eta = 0.3$, γ is relatively small. In Taylor-Couette turbulence, the dimensionless angular velocity flux Nu_ω also increases as η increases, reaching saturation when $\eta \gtrsim 0.7$ [31]. So for flow in rotating cylindrical annulus system, there may exist a unified law that transport efficiency is higher in the system with larger η. In figure 7(a), we plot the normalized Nu (normalized by Nu at $\eta = 0.9$ for the respective Ra) as a function of η. It is clearly seen that Nu decreases with the decrease of η for each Ra. For the case of $\mathrm{Ra} = 10^8$ and $\eta = 0.3$, Nu is only about 70% of that at $\eta = 0.9$. What is the physical reason for the η dependence of heat transport?

As mentioned in § 3.1, the decrease of η results in stronger zonal flow. One possible reason is that thermal plumes are swept away by the shear of zonal flow. Thus, the heat transport is depressed. We adopt the bulk Richardson number $\mathrm{Ri} = \mathrm{Ra}/(\mathrm{Re}^2\,\mathrm{Pr})$ to investigate the competition between the buoyancy and shear effects and analyze the effect of the zonal flow shear by Reynolds number $\mathrm{Re} = \langle u_\phi \rangle_{V,t} L/\nu$. As shown in figure 7(b), it is found that the minimum Ri is 172 corresponding to $\mathrm{Ra} = 10^7$ and $\eta = 0.4$. From the φz temperature field at the mid-radius position (see figure 7(c)), it is found that the main flow structure resembles the bulk flow found in RB convection. Note that elongated streaks along the shear flow do not exist for this maximum shear effects case, which suggests that the flow is dominated by the buoyancy. Recently, Blass et al. [44] have added shearing effects to classical RBC by pulling the top and bottom plates in opposite directions, i.e. the so-called Couette-RB flow. According to the behaviour of the flow structures versus Ri and Re, they considered the flow states are divided into three regimes, including buoyancy dominated regime, transitional regime and shear dominated regime. In ACRBC, Ri is larger than the order of $O(100)$ and Re is no more than 300. So the flow is in the buoyancy dominated regime. From the figure 5(b) of [44], we can estimate that the reduction of Nu is only about 3% for $\mathrm{Re} = 300$ at $\mathrm{Ra} = 10^8$ by linear interpolation. Thus, the shear effect of zonal flow can inhibit heat transfer, but the effect is very weak. We consider that the decrease of heat transport for small η may be due to the geometric confinement effects primarily, which needs to be further studied.

We also investigate the effects of radius ratio on the heat transport from the perspective of plumes. Employing the method introduced in [29, 45–47], the cold plume coverage at the edge of the thermal BL of the outer cylinder is obtained. Figures 8(a) and (b) display the temperature field near the outer surface for $\eta = 0.4$ and 0.9, respectively. It is evident that when $\eta = 0.9$, the area of cold plumes is larger. Figure 8(c) shows ensemble-averaged portion of area $A_{pl}/(L_\phi L_z)$ covered by the cold plumes in the vicinity of the outer surface. As η decreases, a smaller portion of

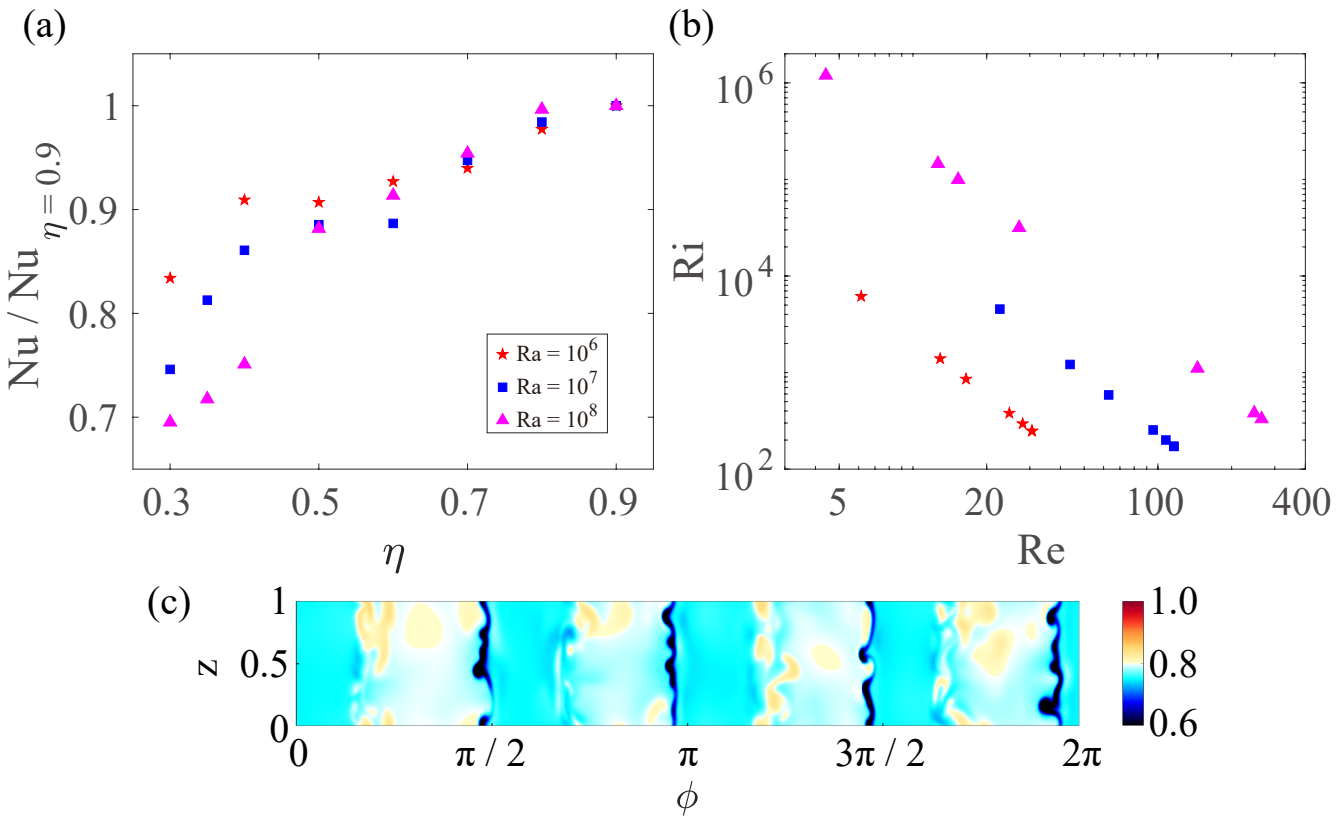

FIG. 7: (a) $\mathrm{Nu}/\mathrm{Nu}_{\eta=0.9}$ as a function of η for different Ra. Here $\mathrm{Nu}/\mathrm{Nu}_{\eta=0.9}$ denotes Nusselt number normalized by the value at $\eta = 0.9$ for the respective Ra. (b) Ri versus Re for different Ra. (c) Instantaneous snapshots of temperature field at mid-radius position for $\mathrm{Ra} = 10^7$ and $\eta = 0.4$.

cold plumes can travel to the opposing BL. Consequently, temperature fluctuations of the thermal BL of the outer surface are smaller (see figure 8(d)) and the heat transfer efficiency is declined.

Asymmetric mean temperature fields

In classical RBC, due to the Oberbeck-Boussinesq (OB) approximation [48], it is generally assumed that the fluid properties are constant, except for the linear variation of the density with temperature in the buoyancy term. However, when the temperature difference Δ between the hot and cold walls is large enough, the drastic changing of fluid properties should be taken into consideration. In this situation, the top-bottom symmetry of the system is broken and the bulk temperature θ_c deviates from the arithmetic mean temperature of hot and cold walls θ_m, which is known as non-Oberbeck-Boussinesq (NOB) effects [49, 50].

Although we implement Oberbeck-Boussinesq approximation in the numerical simulations of ACRBC, remarkable deviation of θ_c from θ_m is observed, which is similar to the NOB effects. Figure 9(a) shows the radial temperature profiles averaged azimuthally, axially and over time. It is evident that θ_c is much larger than θ_m. With η increasing, the deviation $(\theta_c - \theta_m)/\Delta$ decreases for each Ra (see figure 9(b)), which illustrates that the mean temperature profile gradually behaves similarly to the classical RBC. We also perform some experiments in ACRBC system. Details about the experimental setup are introduced in [17]. A small thermistor (Measurement Specialties, GAG22K7MCD419, with a response time of 30 ms in liquids) is inserted into the bulk flow to measure θ_c. Another type of thermistors (Omega, 44131) evenly distributed along the circumferential direction in the cylinders are used to obtain θ_m. $(\theta_c - \theta_m)/\Delta$ at $\eta = 0.5$ for experiments are slightly larger than the cases of DNS, which probably results from the relatively large Ra

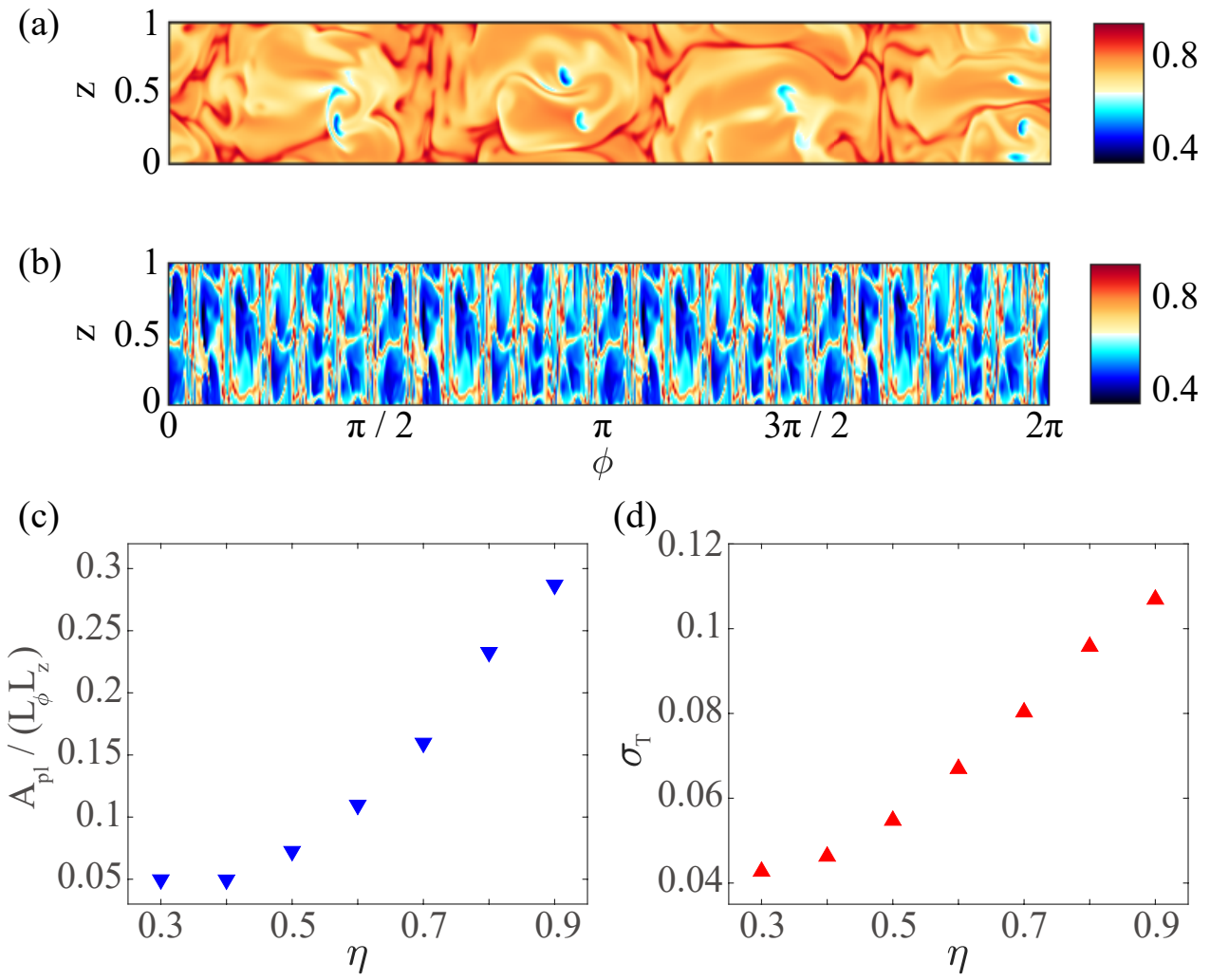

FIG. 8: (a) Instantaneous temperature fields in ϕz-plane at the edge of the thermal BL ($r_\delta = R_o - \delta_T$) for $\eta = 0.4$ (a), 0.9 (b) at $\mathrm{Ra} = 10^7$, where δ_T is the thickness of thermal BL obtained using the slope method [52]. (a) and (b) share the same colorbar. (c) Ensemble-averaged area of cold plumes normalized by the total area versus η. (d) Ensemble-averaged standard deviation of temperature at the position of r_δ versus η.

and Ro^{-1} for experiments ($\mathrm{Ra} = 6 \times 10^{10}$, $\mathrm{Pr} = 4.3$ and $\mathrm{Ro}^{-1} = 18$).

Next, we provide a theoretical explanation for the increase of the deviation $(\theta_c - \theta_m)/\Delta$ with η decreasing. Since the area of the outer cylinder is larger than that of the inner cylinder, according to Fourier's law, the temperature gradient near the outer wall is smaller. Therefore, θ_c (the temperature at the mid-radius position) is slightly higher than θ_m for pure thermal conduction state in ACRBC, indicated by the solid line in figure 9(b). While curvature effect of ACRBC accounts for a part of $(\theta_c - \theta_m)/\Delta$, the difference from the total deviation is still finite. To analytically access $(\theta_c - \theta_m)/\Delta$ observed in DNS and experiments, we first assume that heat is purely transported by conduction in the thin thermal boundary layers. According to the definition of Nu, heat flux conservation through cylindrical surfaces then yields

$$\eta \frac{\Delta\theta^i}{\lambda^i} = \frac{\Delta\theta^o}{\lambda^o} \ , \tag{6}$$

where the thermal boundary layer near the inner (outer) wall is assumed to be a conduction profile with a temperature difference $\Delta\theta^i$ ($\Delta\theta^o$) over a thickness λ^i (λ^o). Note that different curvatures of the two cylinders are considered in the definition of Nu. As shown in figure 9(a), the bulk fluid is isothermal basically (for small η, the slight overshoot of

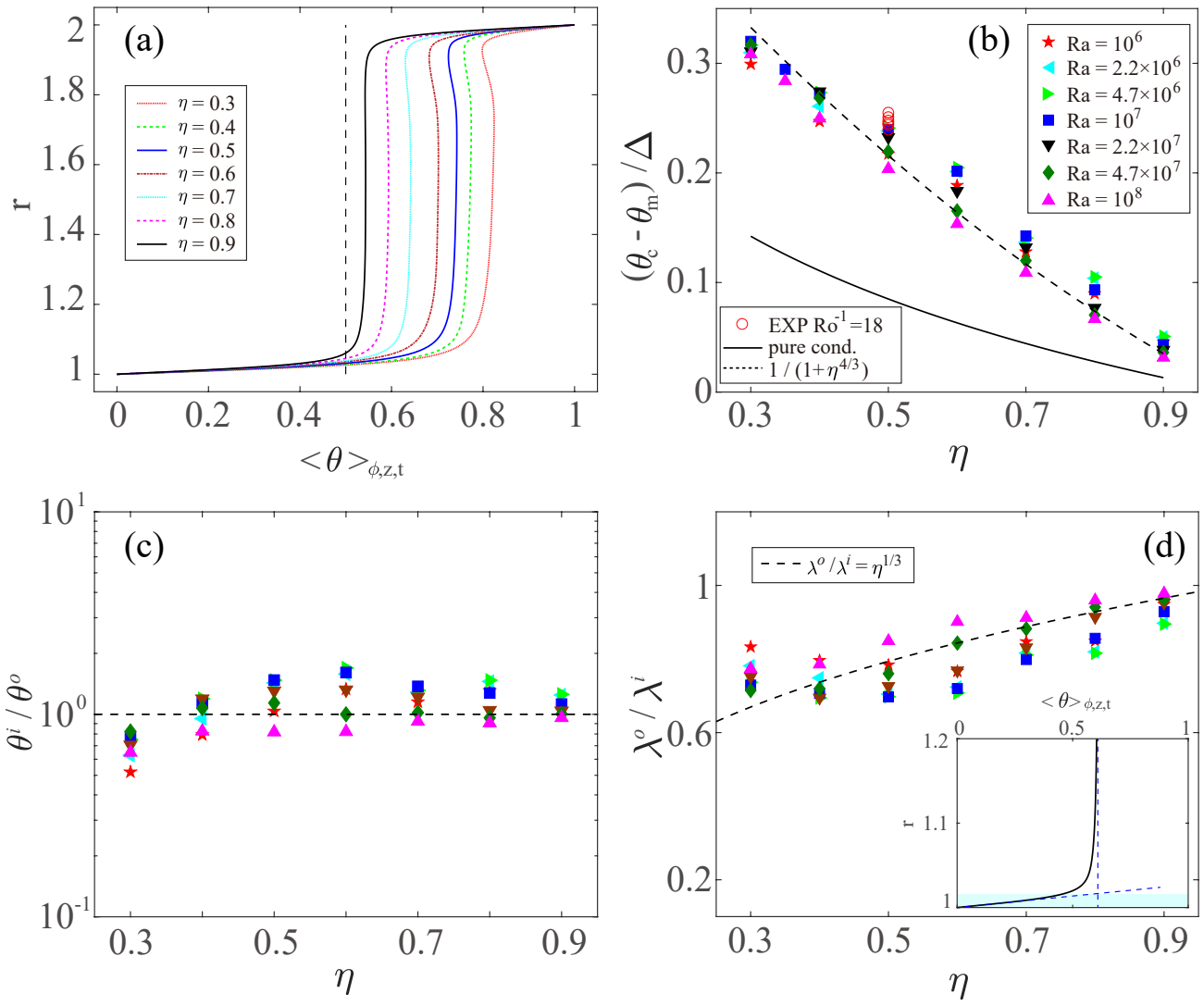

FIG. 9: (a) Azimuthally, axially and time-averaged radial temperature profiles for different η at Ra $= 10^7$. (b) Relative deviation of the bulk temperature (θ_c) from arithmetic mean temperature (θ_m) of the two cylinders $(\theta_c - \theta_m)/\Delta$ versus η for different Ra from DNS (the solid symbols), experiments (the open symbols), and the theoretical prediction given in (9) (dashed line). The experiments are performed at $\eta = 0.5$, Ra $= 6 \times 10^{10}$, Pr $= 4.3$ and $\mathrm{Ro}^{-1} = 18$. The solid line denotes $(\theta_c - \theta_m)/\Delta$ in pure thermal conduction state for comparison. (c) Ratio of boundary layer temperature scales θ^i/θ^o versus η for different Ra. The horizontal dashed line corresponds to the hypothetical identity $\theta^i = \theta^o$ (see (8)). (d) Ratio of thermal boundary layer thicknesses. The dashed line corresponds to the theoretical prediction given in (11). The inset of (d) shows the inner thermal boundary layers λ^i highlighted by the blue shaded area. $\lambda^{i,o}$ are defined as the distances where the tangents of the temperature profiles at the plate cross $\langle\theta\rangle_{\phi,z,t} = \theta_c$.

temperature near the outer surface may result from the effect of Coriolis effects). Thus, we can further assume that the temperature drops occur only in the boundary layers:

$$\Delta\theta^i + \Delta\theta^o = 1\ . \tag{7}$$

Equations (6) and (7) are not sufficient to determine the three unknowns $\Delta\theta^i$, $\Delta\theta^o$ and λ^i/λ^o. So an additional physical assumption is required.

Wu & Libchaber [49], Zhang et al. [51], Gastine et al. [52] proposed that the thermal boundary layers adjust their length scales so that the mean hot and cold temperature fluctuations are equal in the bulk region. Temperature

fluctuations in the bulk region are caused by plumes detaching from the boundary layers. So this implies the equality of the temperature scales for the two boundary layers ($\theta^{i,o} \equiv (\nu\kappa)/(\alpha g_{i,o}(\lambda^{i,o})^3)$). This third assumption yields

$$\theta^i = \theta^o \rightarrow \frac{\nu\kappa}{\alpha g_i (\lambda^i)^3} = \frac{\nu\kappa}{\alpha g_o (\lambda^o)^3} \ , \tag{8}$$

where the centrifugal acceleration $g = \omega^2 r$, so $\chi_g = g(R_i)/g(R_o) = \eta$ reflects radially-dependent gravity effects. Figure 9(c) shows θ^i/θ^o for different η and Ra. Compared to turbulent RB convection in spherical shells reported by Gastine et al. [52] (see their figure 5(a)), the identity of the boundary layer temperature scale is better fulfilled in ACRBC. The temperature drops at both boundaries and the ratio of the thermal BL thicknesses can then be derived using (6)-(8)

$$\Delta\theta^i \simeq \theta_c = \frac{1}{1 + {\chi_g}^{1/3}\eta} = \frac{1}{1+\eta^{4/3}} \ , \tag{9}$$

$$\Delta\theta^o = \frac{1}{1+\eta^{-4/3}} \ , \tag{10}$$

$$\lambda^o/\lambda^i = \eta^{1/3} \ , \tag{11}$$

Figure 9(b) shows that the predicted value (9) and the actual values for mean bulk temperature are in good agreement. We adopt the slope method to define the thickness of thermal boundary layer λ as the distance where the tangent of the temperature profiles at the plate intersects $\langle\theta\rangle_{\phi,z,t} = \theta_c$ (see the inset of figure 9(d)). Figure 9(d) shows that the theory (11) can also predict the asymmetry of the thermal boundary layers λ^o/λ^i. In a word, the theory accurately accounts for the bulk temperature and the boundary layer asymmetry for different η observed in ACRBC. The asymmetry is likely caused by the curvature effects (6) and radially-dependent centrifugal force (8). We note that, although asymmetric mean temperature fields exist in ACRBC, their influence on global heat transport has been shown to be negligible [17].

CONCLUSION

We present an analysis of the zonal flow, heat transport and asymmetric mean temperature field in Annular Centrifugal Rayleigh-Bénard Convection, by means of high-resolution 3D DNS, with radius ratio η varying from 0.3 to 0.9, Ra varying from 10^6 to 10^8, and Pr, Ro^{-1} fixed at 4.3 and 1, respectively. Major findings are summarized as follows:

Firstly, convection rolls move counterclockwise around the axis with a faster rotation rate than the background rotation of ACRBC system. Coriolis force results in the similar deflected angle of hot and cold plumes. Because of the different curvatures of the inner and outer cylinders, the hot plumes can directly affect the ejecting position of the cold plumes, while the impact of the cold plumes does not directly affect the hot plumes. The asymmetric motions of cold and hot plumes push the overall flow to move in the same direction of the background rotation. This mechanism of zonal flow is verified by the variation of the flow behaviour with radius ratio. We observe the drift frequency decreases with η increasing. It is also found that $\langle v_\phi\rangle_{V,t}$ decreases as η increases for each Ra. In addition, zonal flow is the strongest at moderate Ra ($\mathrm{Ra} = 10^7$), which suggests zonal flow is related to the balance of Coriolis force and buoyancy.

Secondly, the scaling exponent of global heat transport γ is 0.28±0.01 for $\eta = 0.3$, 0.4, and transitions to 0.32±0.02 for $\eta \gtrsim 0.5$. The dependence of transport efficiency on η is consistent with Taylor-Couette flow. Furthermore, $\mathrm{Nu}/\mathrm{Nu}_{\eta=0.9}$ decreases with the decrease of η for each Ra. By analyzing the flow field and the ratio of buoyancy and shear effects, it is found that the flow is in the buoyancy dominated regime and the influence of shear effects of zonal

flow on heat transfer is not strong. Additionally, we observed that the cold plume coverage at the edge of the thermal BL of the outer cylinder becomes smaller as η decreases.

Thirdly, the bulk temperature θ_c is found to be much higher than θ_m (0.5) by DNS and experiments. The relative deviation $(\theta_c - \theta_m)/\Delta$ increases with the decrease of η for each Ra. The results of numerical simulations and experiments are consistent, even though the values of Ra and Ro^{-1} are distinct. By assuming pure conduction in the thermal BLs, isothermal bulk fluid, and the equality of the temperature scales for the two boundary layers, we analytically obtain the mean bulk temperature and the ratio of the thickness of the BLs, which are in good agreement with the actual values. The asymmetric mean temperature fields may result from curvature effects and the radially-dependent centrifugal force involved in the hypotheses of the theory.

In the laboratory experiment, centrifugal buoyancy can be larger than Earth's gravity by the rapid rotation of ACRBC. Hypergravitational thermal convection is a new method to achieve high Ra [17]. Systematic study on the dependence of turbulent flow structures and heat transport on radius ratio is urgently needed to understand the flow dynamics in ACRBC. The physical mechanism of zonal flow may improve understanding of some flow phenomena in astrophysical and geophysical settings. Furthermore, the bulk temperature can be significantly increased in the hypergravitational thermal convection system by reducing η, which give insights for the flow and temperature control in engineering applications.

Acknowledgements

This work was supported by the Natural Science Foundation of China (Grant Nos. 11988102, 91852202, 11861131005) and Tsinghua University Initiative Scientific Research Program (Grant No. 20193080058).

Appendix

Table I provide the simulation parameters which are illustated in the subsection of 'Direct numerical simulations'. Movie1, Movie2 and Movie3 are the temperature fields on a ϕr-plane at the mid-axial position for $\eta = 0.3$, 0.6 and 0.9 at $\mathrm{Ra} = 10^7$, $\mathrm{Ro}^{-1} = 1$ and $\mathrm{Pr} = 4.3$, respectively.

$No.$	η	Ra	Δ_g/η_K	N_{tBL}	N_{vBL}	τ_{avg}	Nu	ϵ_{Nu}	Γ	ϕ_0	$N_\phi \times N_z \times N_r$
1	0.3	1.0×10^6	0.24	16	17	255	6.12	0.67%	1	1	$1024 \times 128 \times 128$
2	0.3	2.2×10^6	0.31	13	12	152	7.68	1.09%	1	1	$1024 \times 128 \times 128$
3	0.3	4.7×10^6	0.40	11	13	377	9.39	0.90%	1	1	$1024 \times 128 \times 128$
4	0.3	1.0×10^7	0.51	12	17	247	11.41	0.79%	1	1	$1024 \times 128 \times 128$
5	0.3	2.2×10^7	0.46	17	22	105	14.46	0.57%	0.5	1/2	$960 \times 96 \times 192$
6	0.3	2.2×10^7	0.35	24	25	108	14.20	1.36%	0.25	1/2	$1024 \times 64 \times 256$
7	0.3	4.7×10^7	0.58	15	17	181	17.88	0.15%	0.5	1/2	$960 \times 96 \times 192$
8	0.3	1.0×10^8	0.57	18	19	101	22.37	1.26%	0.25	1/2	$1024 \times 64 \times 256$
9	0.4	1.0×10^6	0.25	16	13	122	6.69	1.23%	1	1	$1408 \times 128 \times 128$
10	0.4	2.2×10^6	0.32	14	16	282	8.42	0.70%	1	1	$1408 \times 128 \times 128$
11	0.4	4.7×10^6	0.41	13	16	179	10.28	0.90%	1	1	$1408 \times 128 \times 128$
12	0.4	1.0×10^7	0.53	11	13	1306	13.14	0.01%	1	1	$1408 \times 128 \times 128$
13	0.4	2.2×10^7	0.47	16	19	205	15.88	0.60%	0.5	1	$2112 \times 96 \times 192$
14	0.4	4.7×10^7	0.61	14	17	641	19.99	0.58%	0.5	1	$2112 \times 96 \times 192$
15	0.4	1.0×10^8	0.59	17	23	136	23.95	1.51%	0.5	1/2	$1280 \times 128 \times 256$
16	0.5	1.0×10^6	0.25	18	19	105	6.66	1.33%	1	1	$1536 \times 128 \times 128$
17	0.5	2.2×10^6	0.40	11	13	521	8.28	0.49%	1	1	$1212 \times 102 \times 102$
18	0.5	4.7×10^6	0.52	9	12	786	10.86	0.12%	1	1	$1212 \times 102 \times 102$
19	0.5	1.0×10^7	0.54	11	13	200	13.54	0.20%	1	1	$1536 \times 128 \times 128$
20	0.5	2.2×10^7	0.56	12	16	333	17.21	0.74%	1	1	$1944 \times 162 \times 162$
21	0.5	4.7×10^7	0.62	13	17	540	21.79	0.25%	0.5	1/2	$1152 \times 96 \times 192$
22	0.5	1.0×10^8	0.62	15	20	166	28.33	0.59%	0.25	1/2	$1536 \times 64 \times 256$
23	0.5	1.0×10^8	0.62	15	20	711	28.04	1.45%	1	1	$3072 \times 256 \times 256$
24	0.6	1.0×10^6	0.25	17	16	416	6.80	0.31%	1	1/2	$1024 \times 128 \times 128$
25	0.6	2.2×10^6	0.33	15	16	381	8.52	0.05%	1	1/2	$1024 \times 128 \times 128$
26	0.6	4.7×10^6	0.42	13	15	351	10.68	0.49%	1	1/2	$1024 \times 128 \times 128$
27	0.6	1.0×10^7	0.55	11	13	654	13.56	0.21%	1	1/2	$1024 \times 128 \times 128$
28	0.6	2.2×10^7	0.49	15	20	341	17.40	1.05%	1	1/2	$1536 \times 192 \times 192$
29	0.6	4.7×10^7	0.64	12	18	389	22.38	0.33%	1	1/2	$1536 \times 192 \times 192$
30	0.6	1.0×10^8	0.63	15	21	305	29.35	0.14%	0.25	1/4	$1024 \times 64 \times 256$
31	0.6	1.0×10^8	0.64	14	19	161	30.95	0.90%	0.25	1/2	$2048 \times 64 \times 256$
32	0.7	1.0×10^6	0.25	17	20	714	6.90	0.06%	1	1/4	$768 \times 128 \times 128$
33	0.7	2.2×10^6	0.33	15	17	528	8.63	0.47%	1	1/4	$768 \times 128 \times 128$
34	0.7	4.7×10^6	0.42	13	16	711	10.74	0.07%	1	1/4	$768 \times 128 \times 128$
35	0.7	1.0×10^7	0.56	10	14	664	14.48	0.36%	1	1	$2560 \times 128 \times 128$
36	0.7	2.2×10^7	0.51	14	19	349	19.22	0.04%	1	1/4	$1152 \times 192 \times 192$
37	0.7	4.7×10^7	0.65	12	16	439	24.29	1.19%	1	1/4	$1152 \times 192 \times 192$
38	0.7	1.0×10^8	0.64	15	22	145	30.65	0.62%	1	1/4	$1280 \times 256 \times 256$
39	0.8	1.0×10^6	0.39	10	12	1013	7.17	0.03%	1	1	$2512 \times 82 \times 82$
40	0.8	2.2×10^6	0.50	8	10	678	9.13	0.04%	1	1	$2512 \times 82 \times 82$
41	0.8	4.7×10^6	0.54	9	10	228	11.79	0.65%	1	1	$3132 \times 102 \times 102$
42	0.8	1.0×10^7	0.56	10	13	461	15.05	0.13%	1	1	$3968 \times 128 \times 128$
43	0.8	2.2×10^7	0.49	15	20	228	19.95	0.86%	0.5	1/4	$1624 \times 102 \times 204$
44	0.8	4.7×10^7	0.62	12	18	249	25.06	0.46%	0.5	1/4	$1624 \times 102 \times 204$
45	0.8	1.0×10^8	0.65	14	21	381	32.01	0.51%	0.25	1/4	$2048 \times 64 \times 256$
46	0.9	1.0×10^6	0.26	17	19	199	7.31	1.73%	1	1/8	$1024 \times 128 \times 128$
47	0.9	2.2×10^6	0.34	15	17	223	9.19	1.50%	1	1/8	$1024 \times 128 \times 128$
48	0.9	4.7×10^6	0.44	12	17	233	11.80	1.36%	1	1/8	$1024 \times 128 \times 128$
49	0.9	1.0×10^7	0.56	10	13	178	15.29	0.94%	1	1/4	$1984 \times 128 \times 128$
50	0.9	2.2×10^7	0.50	14	19	363	18.74	0.16%	1	1/8	$1536 \times 192 \times 192$
51	0.9	4.7×10^7	0.65	12	19	499	23.70	0.23%	1	1/8	$1536 \times 192 \times 192$
52	0.9	1.0×10^8	0.65	14	21	85	32.13	0.11%	0.25	1/4	$4096 \times 64 \times 256$

TABLE I: Simulation parameters. The columns from left to right indicate the followings: radius ratio η, Rayleigh number Ra, the maximum grid spacing Δ_g compared with the Kolmogorov scale estimated by the global criterion $\eta_K = \frac{L \mathrm{Pr}^{1/2}}{[\mathrm{Ra}(\mathrm{Nu}-1)]^{1/4}} \cdot [\frac{(1+\eta)\ln(\eta)}{2(\eta-1)}]^{1/4}$ [17], the number of grid points within the thermal BL N_{tBL} and viscous BL N_{vBL}, the averaging time period τ_{avg}, Nusselt number Nu, the difference of Nu between inner and outer walls $\epsilon_{Nu} = |\mathrm{Nu_{in}} - \mathrm{Nu_{out}}|/\mathrm{Nu}$, aspect ratio Γ, reduced azimuthal domain ϕ_0, the resolution in azimuthal, axial, and radial directions $N_\phi \times N_z \times N_r$.

* jhcthu@foxmail.com

[1] Mckenzie, D.P., Roberts, J.M. & Weiss, N.O. 1974 Convection in the earth's mantle: towards a numerical simulation. *J. Fluid Mech.* **62** (3), 465–538.

[2] Cardin, P. & Olson, P. 1994 Chaotic thermal convection in a rapidly rotating spherical shell: consequences for flow in the outer core. *Phys. Earth Planet. Inter.* **82** (3), 235 – 259.

[3] Wyngaard, J.C. 1992 Atmospheric Turbulence. *Annu. Rev. Fluid Mech.* **24** (1), 205–234.

[4] Hartmann, D.L., Moy, L.A. & Fu, Q. 2001 Tropical Convection and the Energy Balance at the Top of the Atmosphere. *J. Clim.* **14** (24), 4495.

[5] Cheng, L., Abraham, J., Hausfather, Z. & Trenberth, K.E. 2019 How fast are the oceans warming? *Science* **363**, 128–129.

[6] Michael Owen, J. & Long, C.A. 2015 Review of Buoyancy-Induced Flow in Rotating Cavities. *J. Turbomach.* **137**, 11.

[7] Hide, R. & Mason, P.J. 1975 Sloping convection in a rotating fluid. *Adv. Phys.* **24** (1), 47–100.

[8] Bohn, D., Deuker, E., Emunds, R. & Gorzelitz, V. 1995 Experimental and Theoretical Investigations of Heat Transfer in Closed Gas-Filled Rotating Annuli. *J. Turbomach.* **117** (1), 175–183.

[9] Ahlers, G., Grossmann, S. & Lohse, D. 2009 Heat transfer and large scale dynamics in turbulent Rayleigh-Bénard convection. *Rev. Mod. Phys.* **81**, 503–537.

[10] Lohse, D. & Xia, K.-Q. 2010 Small-Scale Properties of Turbulent Rayleigh-Bénard Convection. *Annu. Rev. Fluid Mech.* **42** (1), 335–364.

[11] Chillà, F. & Schumacher, J. 2012 New perspectives in turbulent Rayleigh-Bénard convection. *Eur. Phys. J. E* **35** (7), 1 – 25.

[12] Xia, K.-Q. 2013 Current trends and future directions in turbulent thermal convection. *Theor. and Appl. Mech. Lett.* **3** (5), 052001.

[13] Zou, H.-Y., Zhou, W.-F., Chen, X., Bao, Y., Chen, J. & She, Z.-S. 2019 Boundary layer structure in turbulent Rayleigh-Bénard convection in a slim box. *Acta Mech. Sin.* **35**, 713–728.

[14] Yu, Y., Liu, F., Zhou, T., Gao, C. & Liu, Y. 2019 Numerical solutions of 2-D steady compressible natural convection using high-order flux reconstruction. *Acta Mech. Sin.* **35**, 401–410.

[15] Chen, X., Wang, D.-P. & Xi, H.-D. 2020 Reduced flow reversals in turbulent convection in the absence of corner vortices. *J. Fluid Mech.* **891**, R5.

[16] Kang, C., Meyer, A., Yoshikawa, H.N. & Mutabazi, I. 2019 Numerical study of thermal convection induced by centrifugal buoyancy in a rotating cylindrical annulus. *Phys. Rev. Fluids* **4**, 043501.

[17] Jiang, H., Zhu, X., Wang, D., Huisman, S.G. & Sun, C. 2020 Supergravitational turbulent thermal convection. *Sci. Adv.* **6**, eabb8676.

[18] Rouhi, A., Lohse, D., Marusic, I., Sun, C. & Chung, D. 2021 Coriolis effect on centrifugal buoyancy-driven convection in a thin cylindrical shell. *J. Fluid Mech.* **910**, A32.

[19] Busse, F.H. & Carrigan, C.R. 1974 Convection induced by centrifugal buoyancy. *J. Fluid Mech.* **62** (3), 579–592.

[20] Azouni, M.A., Bolton, E.W. & Busse, F.H. 1985 Convection driven by centrifugal bouyancy in a rotating annulus. *Geophys. Astrophys. Fluid Dyn.* **34** (1-4), 301–317.

[21] Busse, F.H. & Or, A.C. 1986 Convection in a rotating cylindrical annulus: thermal Rossby waves. *J. Fluid Mech.* **166**, 173–187.

[22] Busse, F.H. 1994 Convection driven zonal flows and vortices in the major planets. *Chaos* **4** (2), 123–134.

[23] Yano, J.-I., Talagrand, O. & Drossart, P. 2005 Deep two-dimensional turbulence: An idealized model for atmospheric jets of the giant outer planets. *Geophys. Astrophys. Fluid Dyn.* **99** (2), 137–150.

[24] Heimpel, M., Aurnou, J. & Wicht, J. 2005 Simulation of equatorial and high-latitude jets on Jupiter in a deep convection model. *Nature* **438**, 193–196.

[25] Porco, C.C., West, R.A., McEwen, A., Genio, A.D. Del, Ingersoll, A.P., Thomas, P., Squyres, S., Dones, L., Murray, C.D., Johnson, T.V., Burns, J.A., Brahic, A., Neukum, G., Veverka, J., Barbara, J.M., T.Denk, Evans, M., Ferrier, J.J., Geissler, P., Helfenstein, P., Roatsch, T., Throop, H., Tiscareno, M. & Vasavada11, A.R. 2003 Cassini Imaging of Jupiter's Atmosphere, Satellites, and Rings. *Science* **299**, 1541–1547.

[26] Rhines, P.B. 1975 Waves and turbulence on a beta-plane. *J. Fluid Mech.* **69** (3), 417–443.

[27] Sun, C., Ren, L.-Y., Song, H. & Xia, K.-Q. 2005 Heat transport by turbulent Rayleigh-Bénard convection in 1 m diameter cylindrical cells of widely varying aspect ratio. *J. Fluid Mech.* **542**, 165–174.

[28] van der Poel, E.P., Stevens, R.J.A.M. & Lohse, D. 2011 Connecting flow structures and heat flux in turbulent Rayleigh-Bénard convection. *Phys. Rev. E* **84**, 045303.

[29] Huang, S.-D., Kaczorowski, M., Ni, R. & Xia, K.-Q. 2013 Confinement-Induced Heat-Transport Enhancement in Turbulent Thermal Convection. *Phys. Rev. Lett.* **111**, 104501.

[30] Huang, S.-D. & Xia, K.-Q. 2016 Effects of geometric confinement in quasi-2-D turbulent Rayleigh-Bénard convection. *J. Fluid Mech.* **794**, 639–654.

[31] Grossmann, S., Lohse, D. & Sun, C. 2016 High–Reynolds Number Taylor-Couette Turbulence. *Annu. Rev. Fluid Mech.* **48** (1), 53–80.

[32] Pitz, D.B., Chew, J.W., Marxen, O. & Hills, N.J. 2017 Direct Numerical Simulation of Rotating Cavity Flows Using a Spectral Element-Fourier Method. *J. Eng. Gas Turb. Power* **139** (7).

[33] King, M.P., Wilson, M. & Owen, J.M. 2005 Rayleigh-Bénard Convection in Open and Closed Rotating Cavities. *J. Eng. Gas Turb. Power* **129** (2), 305–311.

[34] Chalghoum, I., Elaoud, S., Kanfoudi, H. & Akrout, M. 2018 The effects of the rotor-stator interaction on unsteady pressure pulsation and radial force in a centrifugal pump. *J. Hydrodyn.* **30** (4), 672–681.

[35] Pitz, D.B., Marxen, O. & Chew, J.W. 2017 Onset of convection induced by centrifugal buoyancy in a rotating cavity. *J. Fluid Mech.* **826**, 484–502.

[36] Verzicco, R. & Orlandi, P. 1996 A Finite-Difference Scheme for Three-Dimensional Incompressible Flows in Cylindrical Coordinates. *J. Comput. Phys.* **123**, 402–414.

[37] van der Poel, E.P., Ostilla-Mónico, R., Donners, J. & Verzicco, R. 2015 A pencil distributed finite difference code for strongly turbulent wall-bounded flows. *Comput. Fluids* **116**, 10–16.

[38] Zhu, X., Phillips, E., Spandan, V., Donners, J., Ruetsch, G., Romero, J., Ostilla, R., Yang, Y., Lohse, D., Verzicco, R., Fatica, M. & Stevens, R.J.A.M. 2018 Afid-gpu: A versatile navier–stokes solver for wall-bounded turbulent flows on gpu clusters. *Comput. Phys. Commun.* **229**, 199–210.

[39] Silano, G., Sreenivasan, K.R. & Verzicco, R. 2010 Numerical simulations of Rayleigh-Bénard convection for Prandtl numbers between 10^{-1} and 10^4 and Rayleigh numbers between 10^5 and 10^9. *J. Fluid Mech.* **662**, 409–446.

[40] Courant, R., Friedrichs, K. & Lewy, H. 1928 Über die partiellen Differenzengleichungen der mathematischen. *Physik. Math. Ann.* **100**, 32–74.

[41] Zhang, Y., Zhou, Q. & Sun, C. 2017 Statistics of kinetic and thermal energy dissipation rates in two-dimensional turbulent Rayleigh–Bénard convection. *J. Fluid Mech.* **814**, 165–184.

[42] Ostilla, R., Stevens, R.J.A.M., Grossmann, S., Verzicco, R. & Lohse, D. 2013 Optimal taylor–couette flow: direct numerical simulations. *J. Fluid Mech.* **719**, 14–46.

[43] Kunnen, R.P.J., Ostilla-Mónico, R., van der Poel, E.P., Verzicco, R. & Lohse, D. 2016 Transition to geostrophic convection: the role of the boundary conditions. *J. Fluid Mech.* **799**, 413–432.

[44] Blass, A., Zhu, X., Verzicco, R., Lohse, D. & Stevens, R.J.A.M. 2020 Flow organization and heat transfer in turbulent wall sheared thermal convection. *J. Fluid Mech.* **897**, A22.

[45] van der Poel, E.P., Verzicco, R., Grossmann, S. & Lohse, D. 2015 Plume emission statistics in turbulent Rayleigh-Bénard convection. *J. Fluid Mech.* **772**, 5–15.

[46] Chong, K.L., Yang, Y., Huang, S.-D., Zhong, J.-Q., Stevens, R.J.A.M., Verzicco, R., Lohse, D. & Xia, K.-Q. 2017 Confined Rayleigh-Bénard, Rotating Rayleigh-Bénard, and Double Diffusive Convection: A Unifying View on Turbulent Transport Enhancement through Coherent Structure Manipulation. *Phys. Rev. Lett.* **119**, 064501.

[47] Jiang, H., Zhu, X., Mathai, V., Verzicco, R., Lohse, D. & Sun, C. 2018 Controlling Heat Transport and Flow Structures in Thermal Turbulence Using Ratchet Surfaces. *Phys. Rev. Lett.* **120**, 044501.

[48] Oberbeck, A. 1879 Ueber die Wärmeleitung der Flüssigkeiten bei Berücksichtigung der Strömungen infolge von Temperaturdifferenzen. *Ann. Phys.-Berlin* **243** (6), 271–292.

[49] Wu, X.-Z. & Libchaber, A. 1991 Non-Boussinesq effects in free thermal convection. *Phys. Rev. A* **43**, 2833–2839.

[50] Yik, H., Valori, V. & Weiss, S. 2020 Turbulent Rayleigh-Bénard convection under strong non-oberbeck-boussinesq conditions. *Phys. Rev. Fluids* **5**, 103502.

[51] Zhang, J., Childress, S. & Libchaber, A. 1997 Non-Boussinesq effect: Thermal convection with broken symmetry. *Phys. Fluids* **9** (4), 1034–1042.

[52] Gastine, T., Wicht, J. & Aurnou, J.M. 2015 Turbulent Rayleigh-Bénard convection in spherical shells. *J. Fluid Mech.* **778**, 721–764.